Chapter 5

Evolution of Quadrupole and Octupole Excitations beyond Noncollective States in ^{114}Te

5.1 Introduction

The existence of vibrational ground state quadrupole bands near the $Z \approx 50$ shell closure is well known and have been extensively studied experimentally, while theoretical model calculations endorsed the underlying physical aspects [145, 146]. However, in due course, the pure vibrational character in some nuclei have been questioned, and later these cases were interpreted to be a result of interplay between γ soft and vibrational character [147–149]. The nuclei are driven to deformation by the excitation of a single or a pair of $g_{9/2}$ protons across the $N = 4$ shell gap. These configurations become energetically favorable owing to the strong proton-pair correlations and residual proton-neutron interactions [150, 151]. However, the interplay of quadrupole excitations and quasiparticle states makes the structure more complex. Based upon total Routhian surface calculations for Te nuclei with $A < 122$, Paul *et al.* [152] predicted weakly deformed collective states ($\beta =$

0.15, $\gamma = 0°$) at low spins. Several non-collective oblate states ($\beta = 0.15$, $\gamma = +60°$) were also observed around medium spin, some of which are even yrast. Non-collective oblate states with a large quadrupole deformation ($\beta = 0.30$) have also been predicted above the yrast states [152–154].

Further, the Te isotopes are known to exhibit collective vibrational features appearing on top of non-collective excitations. A similar phenomenon is observed in other near-spherical nuclei like ^{84}Kr, odd-even Sn, etc. [155]. The quasiparticle phonon model was applied across the isotopic chain in Te nuclei to bring out the systematic understanding of the bands built on proton 6^+ and neutron 8^+ states. The theory predicts both collective and non-collective excitations built upon $[2_1^+ \otimes 6_1^+]_{8^+}$ and $[h_{11/2}]_{8^+}$ configurations respectively, coexisting at similar excitation energy. However, the lack of model data for B($E2$) values of such states made it difficult for the authors to confirm about the degree of collectivity. To validate the claim by Grinberg *et al.* Moller *et al.* [156] investigated ^{114}Te and measured lifetimes of low-lying states. It was concluded that the measured B($E2$) values along the yrast line in ^{114}Te show a rather constant behavior up to $I = 8\hbar$, which looks more like a rotor. A similar observation was also reported in $^{120-124}$Te (See ref. [157]). A similar picture with rotational-like B($E2$) transitions and vibrational-like spectrum is predicted for $N = Z$ nuclei like ^{92}Pd [158]. Therefore, it would be interesting to look for such states and discuss the occurrence of these levels in the framework of shell model calculations.

On the other hand, both Z and N in the neutron-deficient Te isotopes lie close to the deformed octupole magic number 56, and also the combined possibility for a proton-neutron interaction makes the Te isotopes a good candidate for studying the octupole correlation. Enhanced octupole collectivity has been observed in ^{144}Ba with double octupole shell closure $Z = 56$ and $N = 88$ [159]. Further, this property has been studied in $Z \simeq N \simeq 56$ [160–164] and it is found that the observed B($E1$) transition rates ($\approx 10^{-4}$ e^2fm^2) in these nuclei are comparable to those observed in neutron-rich barium ($Z =$

56) nuclei [159], which are an excellent candidate for the octupole correlation with B($E1$)$\sim 10^{-4}$ W.u.. Similar investigations have been carried out in neutron-deficient Te isotopes ($A \approx$ 108-110) [165–167] where octupole correlation has been confirmed based on B($E1$)/B($E2$) ratio.

With this motivation, we planned to investigate the level structure of ^{114}Te both experimentally and theoretically.

5.2 Experimental Details and Data Analysis

The detailed description of the experiment was published in Ref. [25], and are briefly summarized here. The excited states of ^{114}Te were populated by the reaction ^{112}Sn(^{4}He, 2n)^{114}Te at a beam energy of 37 MeV using the K-130 cyclotron accelerator of the Variable Energy Cyclotron Centre, Kolkata. The details of the target are given in the Ref. [168]. The de-excited γ-rays were detected with the seven Compton-suppressed clover HPGe detectors. These detectors were arranged at different angles (θ) with respect to the beam direction; one clover detector at $\theta = 40^{\circ}$, four clover detectors at $\theta = 90^{\circ}$ (two in plane and two out of plane), two clover detectors at $\theta = 125^{\circ}$, and the LEPS detector at $\theta = 40^{\circ}$. The pulse processing and data acquisition system was based on PIXIE-16 12-bit 250 MHz digitizer modules manufactured by XIA LLC and running on firmware conceptualized by UGC-DAE CSR, Kolkata Centre [169]. The multipolarities of the new γ-transitions are determined using the DCO ratio, which is defined as:

$$R_{DCO} = \frac{I\gamma_1 \; at \; 125^{\circ}, \; gated \;\; by \; \gamma_2 \; at \; 90^{\circ}}{I\gamma_1 \; at \; 90^{\circ}, \; gated \;\; by \; \gamma_2 \; at \; 125^{\circ}} \tag{5.1}$$

The value of R_{DCO} for a pure dipole (quadrupole) transition gated by a stretched quadrupole (dipole) transition is 0.7 (1.6). Clover detectors facilitate the linear polarization measurement studies of EM radiation. The polarization asymmetric parameter Δ_{asym} is positive

Table 5.1 The known $E2$ transitions of ^{114}Te and ^{112}Sn nuclei, produced in the present experiment, for which the value of $Q(E_\gamma)$ was measured. These values of $Q(E_\gamma)$ are used to obtain the coefficients a and b as shown in Fig. 5.1.

Nucleus	E_γ (keV)	a_2	a_4	$P(\theta)$	$\triangle_{asym}$	Q
^{114}Te	596.1	0.30 (3)	-0.16 (4)	0.44 (5)	0.13 (2)	0.29 (5)
^{114}Te	708.7	0.28 (2)	-0.10 (3)	0.43 (3)	0.12 (1)	0.27 (3)
^{114}Te	733.7	0.32 (2)	-0.11 (3)	0.51 (3)	0.12 (1)	0.23 (2)
^{114}Te	831.3	0.38 (5)	-0.13 (6)	0.64 (7)	0.13 (2)	0.20 (4)
^{114}Te	901.2	0.38 (9)	-0.22(12)	0.59 (14)	0.12 (2)	0.20 (6)
^{112}Sn	990.5	0.23 (5)	-0.050 (9)	0.37 (6)	0.05 (2)	0.13 (6)
^{112}Sn	1257.2	0.24 (5)	-0.048 (9)	0.38 (6)	0.03 (2)	0.08 (6)

(negative) for electric (magnetic) transitions. The parameter is defined as:

$$\frac{aN_\perp - N_\parallel}{aN_\perp + N_\parallel} \tag{5.2}$$

where $N_\perp$ and $N_\parallel$ are the numbers of scattered photons in a direction perpendicular and parallel to the direction of the reaction plane, respectively. The correction factor a as a function of γ energy comes out to be 1.000(3) (*see*, Fig. 1 in Ref. [25]).

The polarization sensitivity, Q, was also measured. The polarization sensitivity depends on the energy of the γ rays. The polarization sensitivity Q is a measure to characterize a Compton polarimeter and is calculated by using $E2$ transitions of different energies of different residual nuclei populated in the present work (as shown in Table 5.1). The polarization P of those γ transitions are calculated by using the Klein-Nishina formula [99] in which the angular distribution coefficients a_2 and a_4 were taken from the Refs. [156, 170, 171] for ^{114}Te and ^{112}Sn respectively. The linear polarization $P(\theta)$ is related to the polarization asymmetry and polarization sensitivity Q in terms of the following relation:

$$P(\theta) = \frac{\triangle}{Q} \tag{5.3}$$

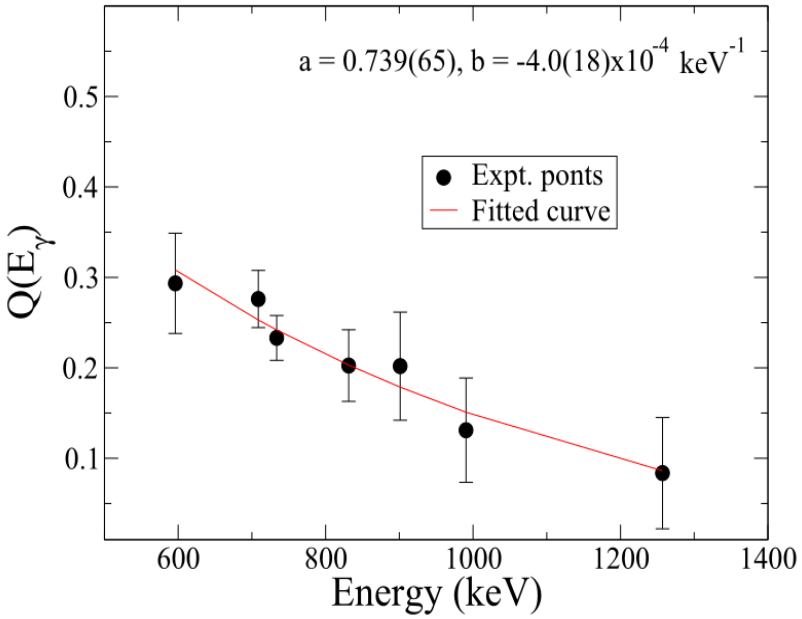

Figure 5.1 Polarization sensitivity of the clover detector placed at the 90° of the INGA array in the present experiment.

Fig. 5.1 represents the fitted curve of the Q parameter using the following relation:

$$Q = Q_0(a + b * E_\gamma) \tag{5.4}$$

where Q_0 represents the polarization sensitivity of an ideal Compton polarimeter and is defined as

$$Q_0 = \frac{1+\alpha}{1+\alpha+\alpha^2} \tag{5.5}$$

with $\alpha = \frac{E_\gamma(keV)}{511}$. The values of the parameters a and b, which are obtained by fitting Eq. 5.4 are 0.739(65) and -4.0(18)$\times 10^{-4}$, keV^{-1} respectively. We have deduced the value of the linear polarization to confirm the J^π assignment of some levels.

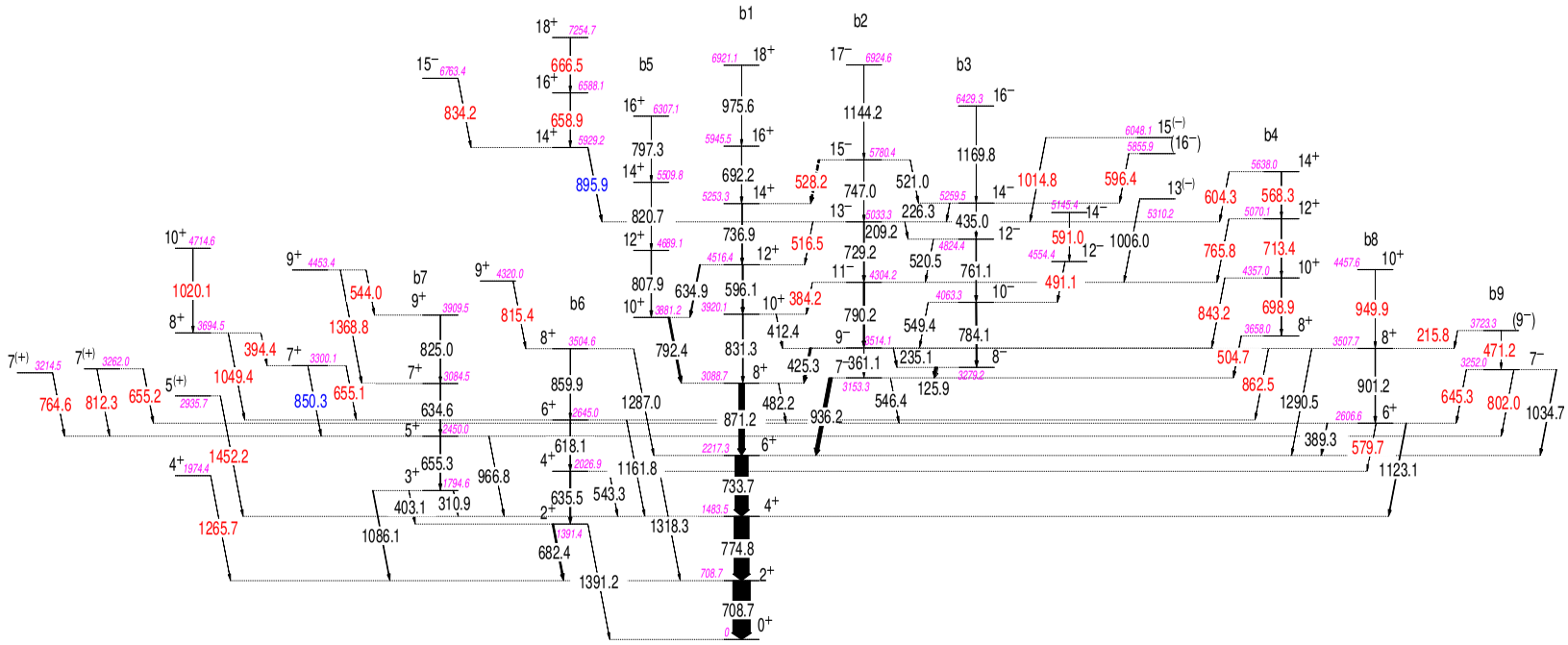

Figure 5.2 Partial level scheme of ^{114}Te based on present work and previous work [25, 170]. The newly observed transitions in the present work are shown in red color. The level energies for each level are represented by magenta color. The transitions marked by blue color are the ones that are already observed in previous work, but the placement of these transitions is modified in the present work.

Table 5.2 List of initial states (E_i) and energies of γ rays (E_γ), spins, relative intensity (I_γ), R_{DCO} values, linear polarization asymmetry (Δ_{asym}), multipole mixing ratio ($\delta_{E2/M1}$), and multipolarity ($E\lambda/M\lambda$) of the γ transition in ^{114} Te.

E_i[#](keV)	E_γ (keV)	$I_i \rightarrow I_f$	I_γ[†]	R_{DCO}	Δ_{asym}	$\delta_{E2/M1}$	$E\lambda/M\lambda$
708.7 (1)	708.7 (1)	$2^+ \rightarrow 0^+$	100.0 (52)	1.02 (10)[a]	0.12 (1)	-	$E2$
1391.4 (2)	682.4 (3)	$2^+ \rightarrow 2^+$	9.28 (47)	0.96 (7)[b]	-0.10 (3)	3.50^{+2950}_{-221} [p]	$M1$+$E2$
	1391.2[⊕](5)	$2^+ \rightarrow 0^+$	0.12 (3)	-	-	-	-
1483.5 (2)	774.8 (1)	$4^+ \rightarrow 2^+$	84.7 (86)	0.98 (9)[b]	0.14 (1)	-	$E2$
1794.6 (2)	310.9 (3)	$3^+ \rightarrow 4^+$	0.91 (13)	0.57 (7)[b]	-	3.70^{+70}_{-60} [q]	$M1$+$E2$
	403.1 (3)	$3^+ \rightarrow 2^+$	0.78 (8)	0.56 (8)[b]	-	-2.54^{+70}_{-52} [q]	$M1$+$E2$
	1086.1 (2)	$3^+ \rightarrow 2^+$	4.11 (42)	0.82 (10)[b]	0.01 (4)	0.29^{+14}_{-11} [q]	$M1$+$E2$
1974.4 (2)	1265.7*(3)	$4^+ \rightarrow 2^+$	0.70 (12)	1.03 (12)[b]	0.05 (2)	-	$E2$
2026.9 (2)	543.3 (4)	$4^+ \rightarrow 4^+$	1.56 (17)	0.83 (6)[b]	-0.07 (4)	-2.60^{+370}_{-112}, 1.40^{+93}_{-39} [p]	$M1$+$E2$
	635.5 (2)	$4^+ \rightarrow 2^+$	7.17 (10)	1.01 (10)[c]	0.14 (3)	-	$E2$
	1318.3 (4)	$4^+ \rightarrow 2^+$	0.85 (10)	0.99 (16)[b]	0.09 (7)	-	$E2$
2217.3 (2)	733.7 (1)	$6^+ \rightarrow 4^+$	74.2 (76)	0.98 (11)[b]	0.12 (1)	-	$E2$
2450.0 (2)	655.3 (2)	$5^+ \rightarrow 3^+$	3.93 (24)	0.97 (11)[b]	0.05 (2)	-	$E2$
	966.8 (5)	$5^+ \rightarrow 4^+$	0.56 (9)	0.58 (9)[b]	-	-3.79^{+317}_{-147} [q]	$M1$+$E2$
2606.6 (2)	389.3 (2)	$6^+ \rightarrow 6^+$	3.83 (24)	0.97 (9)[b]	0.10 (3)	-	$E2$
	579.7*(4)	$6^+ \rightarrow 4^+$	1.19 (14)	1.02 (13)[b]	0.07 (6)	-	$E2$
	1123.1 (3)	$6^+ \rightarrow 4^+$	4.64 (49)	1.02 (10)[a]	0.07 (3)	-	$E2$
2645.0 (2)	618.1 (2)	$6^+ \rightarrow 4^+$	4.11 (42)	0.98 (11)[b]	0.05 (2)	-	$E2$
	1161.8 (5)	$6^+ \rightarrow 4^+$	0.57 (7)	1.01 (12)[b]	-	-	($E2$)
2935.7 (4)	1452.2*(4)	$5^{(+)} \rightarrow 4^+$	0.69 (9)	0.69 (9)[a]	-0.04 (5)	-	($M1$)
3084.5 (3)	634.6 (3)	$7^+ \rightarrow 5^+$	2.14 (26)	0.96 (12)[a]	0.07 (2)	-	$E2$
3088.7 (2)	482.2 (2)	$8^+ \rightarrow 6^+$	1.44 (16)	1.05 (11)[a]	0.08 (4)	-	$E2$
	871.2 (2)	$8^+ \rightarrow 6^+$	33.5 (17)	0.98 (11)[b]	0.13 (7)	-	$E2$
3153.3 (2)	546.4[⊕](4)	$7^- \rightarrow 6^+$	0.24 (6)	-	-	-	-

$E_i^{\#}$(keV)	E_γ (keV)	$I_i \rightarrow I_f$	$I_\gamma^{\dagger}$	R_{DCO}	Δ_{asym}	$\delta_{E2/M1}$	$E\lambda/M\lambda$
	936.2 (2)	$7^- \rightarrow 6^+$	21.0 (11)	0.68 (6)[a]	0.14 (1)	-	$E1$
3214.5 (4)	764.6*,‡ (3)	$7^{(+)} \rightarrow 5^+$	0.88 (22)	0.96 (10)[d]	-	-	($E2$)
3252.0 (3)	645.3*(3)	$7^- \rightarrow 6^+$	0.65 (7)	0.67 (9)[e]	0.06 (5)	-0.06$^{+15}_{-14}$ [q]	$E1$
	802.0*(5)	$7^- \rightarrow 5^+$	-	-	-	-	-
	1034.7 (3)	$7^- \rightarrow 6^+$	3.76 (40)	0.68 (7)[a]	0.09 (3)	-0.10$^{+15}_{-20}$ [p]	$E1$
3262.0 (3)	655.2*,*(3)	$7^{(+)} \rightarrow 6^+$	2.42 (40)	0.74 (15)[e]	-	-	($M1$)
	812.3*(4)	$7^{(+)} \rightarrow 5^+$	0.45 (9)	1.10 (23)[b]	-	-	($E2$)
3279.2 (4)	125.9$^{\alpha}$ (4)	$8^- \rightarrow 7^-$	13.2 (12)	0.50 (5)[a]	0.05 (2)	-0.60$^{+18}_{-17}$ [p]	$M1$+$E2$
3300.1 (4)	655.1*,*(3)	$7^+ \rightarrow 6^+$	0.50 (13)	0.70 (7)[c]	-	-	($M1$)
	850.3 (4)	$7^+ \rightarrow 5^+$	0.93 (16)	1.10 (18)[d]	0.04 (3)	-	$E2$
3504.6 (4)	859.9 (4)	$8^+ \rightarrow 6^+$	0.27 (7)	1.08 (14)[c]	0.07 (6)	-	$E2$
	1287.0$^{\diamond}$ (4)	$8^+ \rightarrow 6^+$	0.40 (15)	-	-	-	-
3507.7 (2)	862.5*(4)	$8^+ \rightarrow 6^+$	0.21 (7)	-	-	-	-
	901.2 (3)	$8^+ \rightarrow 6^+$	3.70 (27)	0.97 (9)[b]	0.12 (2)	-	$E2$
	1290.5$^{\diamond}$ (4)	$8^+ \rightarrow 6^+$	0.84 (11)	-	-	-	-
3514.1 (3)	235.1$^{\bullet}$ (3)	$9^- \rightarrow 8^-$	2.56 (20)	-	-	-	-
	361.1 (4)	$9^- \rightarrow 7^-$	1.87 (18)	1.06 (14)[a]	0.10 (3)	-	$E2$
	425.3 (3)	$9^- \rightarrow 8^+$	11.7 (6)	0.73 (6)[a]	0.12 (1)	0.05$^{+9}_{-7}$ [q]	$E1$
3658.0 (4)	504.7*(3)	$8^+ \rightarrow 7^-$	2.61 (13)	0.67 (7)[a]	0.14 (4)	-0.09$^{+14}_{-10}$ [p]	$E1$
3694.5 (4)	394.4$^{*,\bullet}$(4)	$8^+ \rightarrow 7^+$	0.34 (3)	-	-	-	-
	1049.4*(4)	$8^+ \rightarrow 6^+$	0.81 (10)	1.11 (13)[b]	0.13 (7)	-	$E2$
3723.3 (4)	215.8$^{*,\oplus}$(4)	$(9^-) \rightarrow 8^+$	0.22 (2)	-	-	-	-
	471.2$^{*,\oplus}$(4)	$(9^-) \rightarrow 7^-$	0.20 (3)	-	-	-	-
3881.2 (3)	792.4 (2)	$10^+ \rightarrow 8^+$	10.73 (58)	1.07 (10)[b]	0.14 (3)	-	$E2$
3909.5 (4)	825.0 (3)	$9^+ \rightarrow 7^+$	0.95 (13)	1.04 (11)[b]	0.09 (4)	-	$E2$
3920.1 (2)	412.4 (2)	$10^+ \rightarrow 8^+$	2.11 (12)	0.96 (9)[a]	0.07 (3)	-	$E2$
	831.3 (2)	$10^+ \rightarrow 8^+$	4.98 (26)	1.01 (10)[b]	0.13 (2)	-	$E2$

$E_i^{\#}$(keV)	E_γ (keV)	$I_i \rightarrow I_f$	$I_\gamma{}^{\dagger}$	R_{DCO}	Δ_{asym}	$\delta_{E2/M1}$	$E\lambda/M\lambda$
4063.3 (4)	549.4 (4)	$10^- \rightarrow 9^-$	0.36 (7)	0.50 (8)[a]	0.02 (2)	-0.58^{+28}_{-21} [p]	$M1+E2$
	784.1 (2)	$10^- \rightarrow 8^-$	6.91 (42)	0.97 (10)[b]	0.13 (4)	-	$E2$
4304.2 (4)	384.2$^{*,\oplus}$(5)	$11^- \rightarrow 10^+$	0.48 (2)	0.70 (10)[g]	0.05 (4)	-0.07^{+14}_{-16} [q]	$E1$
	790.2 (3)	$11^- \rightarrow 9^-$	7.93 (39)	1.07 (10)[b]	0.15 (4)	-	$E2$
4320.0 (5)	815.4*(3)	$9^+ \rightarrow 8^+$	0.52 (7)	0.46 (5)[b]	0.04 (3)	-1.3^{+10}_{-7} [p]	$M1+E2$
4357.0 (4)	698.9*(3)	$10^+ \rightarrow 8^+$	1.52 (11)	0.95 (10)[h]	0.11 (5)	-	$E2$
	843.2*(4)	$10^+ \rightarrow 9^-$	1.01 (5)	1.09 (17)[f]	0.05 (4)	-	$E1$
4453.4 (5)	544.0*,‡(5)	$9^+ \rightarrow 9^+$	0.75 (2)	-	-	-	-
	1368.8*(4)	$9^+ \rightarrow 7^+$	1.25 (19)	0.97 (10)[b]	0.06 (5)	-	$E2$
4457.6 (5)	949.9*(4)	$10^+ \rightarrow 8^+$	0.71 (8)	0.98 (12)[a]	0.09 (6)	-	$E2$
4516.4 (4)	596.1$^{\ominus}$ (3)	$12^+ \rightarrow 10^+$	6.64 (39)	0.95 (10)[h]	0.13 (4)	-	$E2$
	634.9 (5)	$12^+ \rightarrow 10^+$	6.13 (25)	0.95 (12)[h]	0.11 (3)	-	$E2$
4554.4 (5)	491.1*(3)	$12^- \rightarrow 10^-$	1.48 (7)	1.58 (18)[f]	0.12 (5)	-	$E2$
4689.1 (5)	807.9 (3)	$12^+ \rightarrow 10^+$	3.57 (26)	1.00 (10)[b]	0.11 (3)	-	$E2$
4714.6 (6)	1020.1*(4)	$10^+ \rightarrow 8^+$	1.10 (12)	1.05 (10)[b]	0.08 (5)	-	$E2$
4824.4 (4)	520.5$^{\ominus}$ (5)	$12^- \rightarrow 11^-$	0.85 (16)	-	-	-	-
	761.1 (3)	$12^- \rightarrow 10^-$	4.40 (22)	0.99 (10)[a]	0.07 (3)	-	$E2$
5033.3 (4)	209.2$^{\bullet}$ (4)	$13^- \rightarrow 12^-$	1.62 (19)	-	-	-	-
	516.5*(4)	$13^- \rightarrow 12^+$	0.62 (5)	0.72 (9)[g]	0.06 (4)	-0.04^{+15}_{-17} [q]	$E1$
	729.2 (4)	$13^- \rightarrow 11^-$	5.48 (35)	1.06 (10)[a]	0.09 (3)	-	$E2$
5070.1 (4)	713.4*(4)	$12^+ \rightarrow 10^+$	0.76 (4)	1.64 (20)[f]	0.08 (5)	-	$E2$
	765.8*(5)	$12^+ \rightarrow 11^-$	0.46 (3)	0.68 (8)[g]	0.08 (7)	-0.10^{+13}_{-14} [q]	$E1$
5145.4 (7)	591.0*(5)	$14^- \rightarrow 12^-$	0.29 (7)	1.58 (24)[f]	0.06 (7)	-	$E2$
5253.3 (5)	736.9 (3)	$14^+ \rightarrow 12^+$	4.52 (37)	0.95 (11)[a]	0.13 (3)	-	$E2$
5259.5 (4)	226.3 (3)	$14^- \rightarrow 13^-$	0.69 (11)	0.49 (4)[a]	0.06 (4)	-0.90^{+83}_{-50} [p]	$M1+E2$
	435.0 (3)	$14^- \rightarrow 12^-$	1.74 (12)	1.02 (11)[a]	0.08 (3)	-	$E2$
5310.2 (5)	1006.0 (5)	$13^{(-)} \rightarrow 11^-$	0.82 (23)	1.10 (13)[b]	-	-	$(E2)$

$E_i^{\#}$(keV)	E_γ (keV)	$I_i \rightarrow I_f$	$I_\gamma^{\dagger}$	R_{DCO}	Δ_{asym}	$\delta_{E2/M1}$	$E\lambda/M\lambda$
5509.8 (6)	820.7 (4)	$14^+ \rightarrow 12^+$	0.94 (14)	1.02 (13)[b]	0.15 (5)	-	$E2$
5638.0° (5)	568.3*(5)	$14^+ \rightarrow 12^+$	0.53 (2)	-	-	-	-
	604.3*(5)	$14^+ \rightarrow 13^-$	0.70 (3)	0.98 (14)[f]	0.09 (7)	-	$E1$
5780.4 (6)	521.0$^{\ominus}$ (5)	$15^- \rightarrow 14^-$	0.85 (16)	-	-	-	-
	528.2	$15^- \rightarrow 14^+$	-	-	-	-	-
	747.0 (4)	$15^- \rightarrow 13^-$	0.95 (7)	0.95 (12)[a]	0.12 (8)	-	$E2$
5855.9 (6)	596.4* (5)	$(16^-) \rightarrow 14^-$	-	-	-	-	-
5929.2 (6)	895.9 (3)	$14^+ \rightarrow 13^-$	2.77 (23)	0.71(7)[a]	0.08 (3)	-0.10^{+16}_{-13} [p]	$E1$
5945.5 (6)	692.2 (4)	$16^+ \rightarrow 14^+$	2.32 (22)	1.04 (11)[b]	0.08 (4)	-	$E2$
6048.1 (6)	1014.8* (5)	$15^{(-)} \rightarrow 13^-$	1.64 (28)	0.94 (9)[b]	-	-	($E2$)
6307.1 (8)	797.3 (5)	$16^+ \rightarrow 14^+$	0.84 (16)	1.04 (11)[h]	0.06 (6)	-	$E2$
6429.3 (7)	1169.8 (5)	$16^- \rightarrow 14^-$	0.58 (8)	1.08 (8) [h]	0.10 (7)	-	$E2$
6588.1 (7)	658.9*(4)	$16^+ \rightarrow 14^+$	1.80 (14)	1.06 (17)[h]	0.11 (5)	-	$E2$
6763.4 (7)	834.2*(4)	$15^- \rightarrow 14^+$	0.74 (10)	0.68 (7)[h]	0.08 (6)	-0.09^{+7}_{-15} [q]	$E1$
6921.1 (8)	975.6$^{\odot}$(5)	$18^+ \rightarrow 16^+$	0.26 (9)	-	-	-	$E2$
6924.6 (8)	1144.2 (5)	$17^- \rightarrow 15^-$	0.45 (8)	1.05 (19)[h]	0.09 (11)	-	$E2$
7254.7 (9)	666.5*(5)	$18^+ \rightarrow 16^+$	0.73 (14)	1.06 (10)[h]	0.09 (8)	-	$E2$

[#] The level energies are obtained by fitting the γ-ray energies using the code GTOL.

† Intensities of γ-transitions are normalized to the 708.7 keV transition, with Iγ = 100.

* Indicates new γ-transitions observed in the present work.

[a]DCO ratios are obtained by gating 774.8 keV stretched quadrupole ($E2$) transition.

[b]DCO ratios are obtained by gating 708.7 keV stretched quadrupole ($E2$) transition.

[c]DCO ratios are obtained by gating 618.1 keV stretched quadrupole ($E2$) transition.

[d]DCO ratios are obtained by gating 655.3 keV stretched quadrupole ($E2$) transition.

[e]DCO ratios are obtained by gating 1123.1 keV stretched quadrupole ($E2$) transition.

[f]DCO ratios are obtained by gating 936.2 keV stretched dipole ($M1$) transition.

[g]DCO ratios are obtained by gating 831.3 keV stretched quadrupole ($E2$) transition.

[h]DCO ratios are obtained by gating 733.7 keV stretched quadrupole ($E2$) transition.

$\oplus$ Multipolarity of these *gamma*-transitions can not be determined due to very weak intensities.

$\ddagger$ $\triangle_{asym}$ of these *gamma*-transitions can not be determined due to the unavailability of clean gate.

$\star$ $\triangle_{asym}$ of these *gamma*-transitions can not be determined due to presence of similar transitions in the present work.

$\diamond$ $\triangle_{asym}$ of these *gamma*-transitions can not be determined due to overlap between the 1287.0- and 1290.5-keV transitions.

$\bullet$ Multipolarity of these γ- transitions can not be determined due to contamination from ^{114}Sb.

$\odot$ Multipolarity of this transition is confirmed from previous work.

$\ominus$ Combined intensity of these transitions are given due to small difference in centroid (521.0- and 520.5-keV, 596.1- and 596.4-keV transitions.

$\circ$ Spin and parity of these level is confirmed by 604.3-keV transitions.

α Contribution of internal conversion coefficient towards intensity is 36% by considering the transition to be $M1$.

[p] mixing ratios are calculated by using linear polarization and DCO values both.

[q] mixing ratios are calculated by using DCO values only.

5.3 Results

The proposed level scheme of ^{114}Te, resulting from the present analysis, is presented in Fig. 5.2. Properties of the transitions and levels determined from this work are reported in Table 5.2. The ground state band b1 has already been reported up to 18^+ spin [170]. The present work confirms already reported transitions in ^{114}Te. At the same time, thirty-five new transitions have been placed across various bands. The 1265.7-keV (Fig. 5.3) transition was found to decay from 1974.4-keV level to the 708.7-keV level of the ground state band. The 1452.2-keV transition (see Fig. 5.3) feeds into the 1483.5-keV level with spin

4^+ . From the DCO and polarization asymmetry, it has been found that the 1265.7-keV transition is a stretched $E2$ character, whereas the 1452.2-keV transition is a dipole in nature.

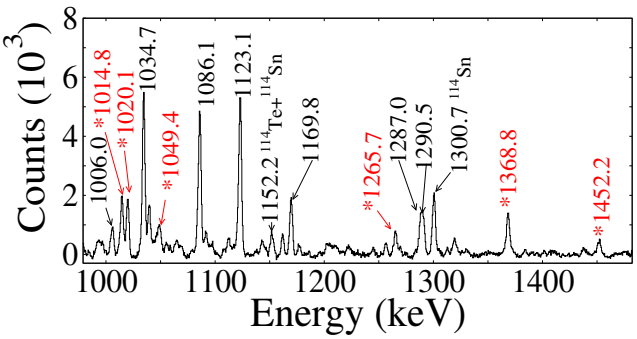

Figure 5.3 Prompt γ-rays observed in coincidence with 708.7-keV transition. The newly observed transitions are indicated by an asterisk in red color.

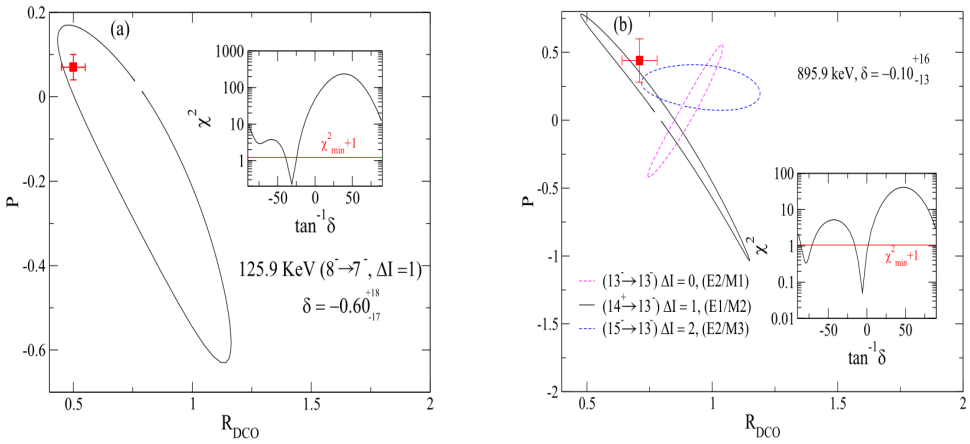

Figure 5.4 The panels (a) and (b) represent the variation of linear polarization (P) as a function of R_{DCO} at different values of δ for 125.9- and 895.9-keV transitions. The inset provides the χ^2 analysis for the corresponding transitions.

On the other hand, the already reported bands b2 and b3 are also observed along with the inter-band transitions. Similar bands are observed in all even-even Te isotopes with A $\approx$ 112-132. These negative parity states are most likely based on two quasi-neutron $\nu h_{11/2}d_{5/2}$ configurations [172]. Based on DCO measurements, the 125.9-, 226.3-, and

549.4-keV transitions feeding from band b3 to band b2 are of mixed type with mixing ratios -0.60 (see Fig. 5.4(a)), -0.90, and -0.58 respectively, whereas the multipolarity of 235.1-, and 209.2-keV transitions decaying from band b2 to band b3 is not reported in the present work due to contamination from ^{114}Sb. A small cascade of γ-rays with energies 491.1 and 591.0 keV (Fig. 5.5) has been observed to feed into the 4063.3-keV level at spin 10^- of band b3. Both are confirmed to be stretched $E2$ transitions.

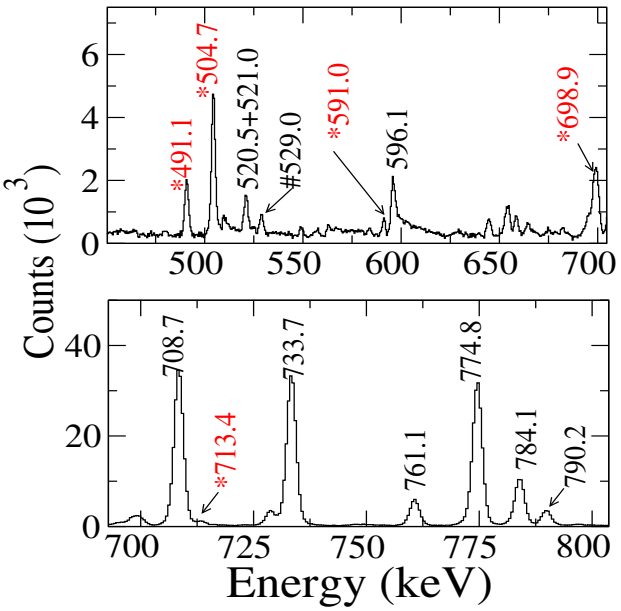

Figure 5.5 The γ-γ coincidence spectra obtained from the gate on 936.2-keV dipole transition. The gamma transition with energy 529.0 keV and highlighted with symbol # belongs to ^{114}Te. However, the placement is doubtful.

The band b2 is interconnected to band b1 with enhanced $E1$ γ-transitions 936.2, 425.3, 384.2, and 516.5 keV (Fig. 5.6). A small sequence of γ-transitions was also observed to feed into the 13^- level of band b2. I. Thorslund *et al.* has placed 895.9-keV transition at spin 18^+ of band b1. In the present work, we have placed this transition at 5033.3 keV level, spin 13^- because this transition did not appear in the coincidence of 736.9-, 692.2-, and 975.6-keV transitions, but it is observed in the coincidence of 729.2-, 790.2, 761.1-, and 784.1-keV transitions. We assigned $E1$ multipolarity to this transition based on DCO

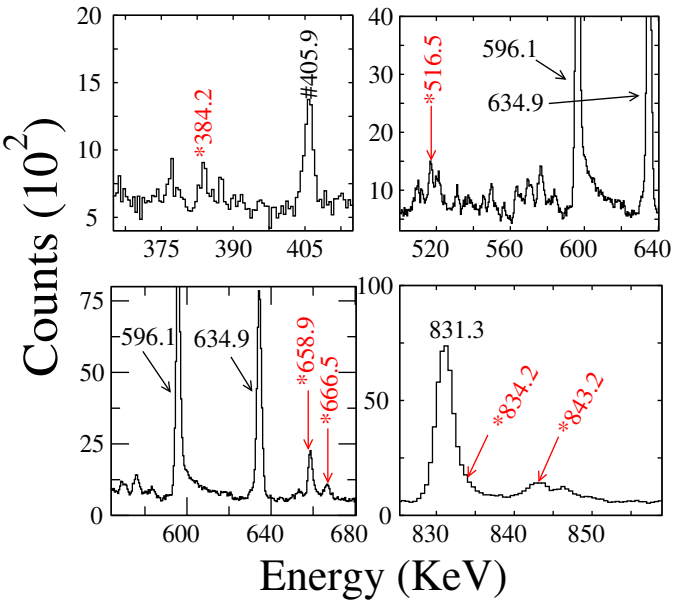

Figure 5.6 Prompt γ-γ coincidence spectra gated by 871.2-keV transition. The 384.2-, 516.5-, 834.2-, and 843.2-keV newly observed transitions are $E1$ in nature. The placement of 405.9 keV gamma transition represented by # symbol could not be resolved in the present work.

and polarization asymmetry measurement. The linear polarization vs R_{DCO} plot confirms the spin of the 895.9-keV transition as shown in Fig. 5.4 (b). A new branch with three new γ-rays decay to band b2 through 895.9-keV transition has been observed. The 834.2-keV (Fig. 5.6) transition is assigned $E1$ multipolarity, whereas $E2$ character was observed for the 658.9-, and 666.5-keV (Fig. 5.6) transitions. A new gamma transition with energy 1014.8 keV was observed to feed into the 5033.3-keV level. This transition was found to be quadrupole in nature on the basis of DCO measurement. Another new gamma transition with energy 596.4 keV was also found to decay to the 5259.5-keV level. We have assigned tentative $E2$ multipolarity to this transition.

A new band termed as b4 has been observed for the first time in the present work. The band contains three transitions with energies 698.9, 713.4, and 568.3 keV (Fig. 5.5). The stretched electric quadruple nature of 698.9- and 713.4-keV transitions are confirmed in our work. The band b4 is connected with band b2 through 504.7-, 843.2-, 765.8-, and

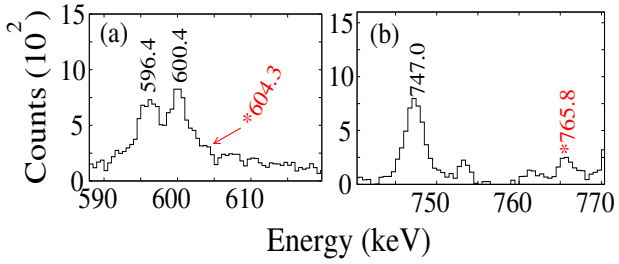

Figure 5.7 The γ-γ coincidence spectra obtained from the gate on 729.2-(a), and 790.2-keV (b) quadrupole transitions showing two newly observed interconnected transitions between bands b4 and b2. it is to be noted that the 596.4 keV gamma is different from 596.1. The 600.4 keV transition is a likely contamination from ^{114}Sb.

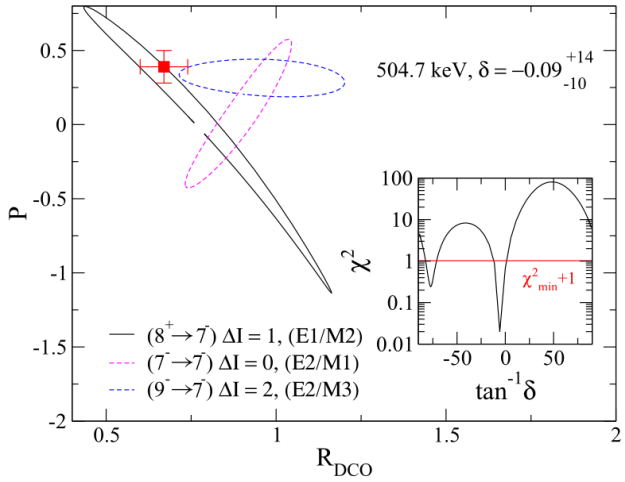

Figure 5.8 The variation of linear polarization as a function of R_{DCO} at different value of δ for 504.7 keV transition. The inset shows the χ^2 vs $\tan^{-1}\delta$ plot giving the mixing ratio δ = -0.09$^{+14}_{-10}$.

604.3-keV (Fig. 5.5, 5.7) transitions. The DCO and polarization measurements confirm the $E1$ nature of 504.7-, 843.2-, and 604.3-keV transitions. We have also confirmed the spin assignment of the band head by plotting the R_{DCO} vs. linear polarization plot for 504.7-keV transition (see Fig. 5.8).

The band b5 has been observed in the previous work up to spin 50^+ [170] and was reported to show smooth band termination. However, this band was observed up to spin 18^+ in the present work. This band decays into band b1 via 792.4 keV stretched $E2$ transition.

The bands b6 and b7 were reported in the previous work and interpreted as γ bands [25]. We have observed some new interleaved transitions that are connected with bands b6 and b7. The 1049.4- and 815.4-keV (Fig.5.3, 5.9) transitions decay to band b6 at level energies 2645.0 and 3504.6 keV, respectively. The 1049.4-keV transition is assigned as $E2$ type whereas, the 815.4-keV transition shows the mixed character with $\delta = -1.73^{+55}_{-75}, -0.51^{+11}_{-40}$ (see Fig. 5.10). To confirm the spin of the level from which the 815.4-keV transition is decaying, the R_{DCO} vs. linear polarization plot has been plotted for different multipolarities. As shown in Fig. 5.11 the value of δ obtained from the R_{DCO}-polarization method gives δ = -1.3$^{+10}_{-7}$.

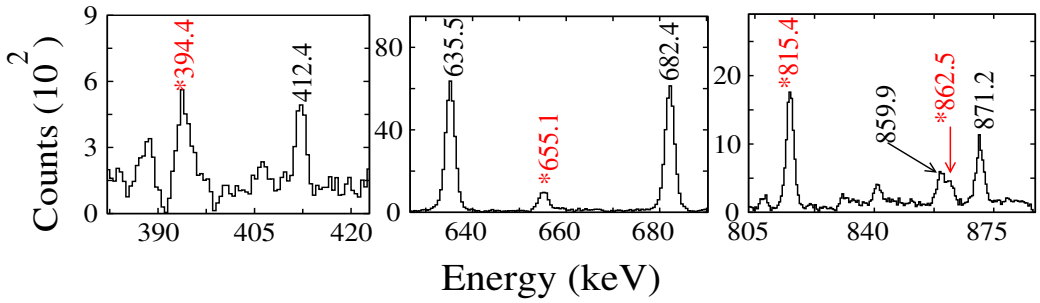

Figure 5.9 Prompt γ-γ coincidence spectra with gate on 618.1-keV transition.

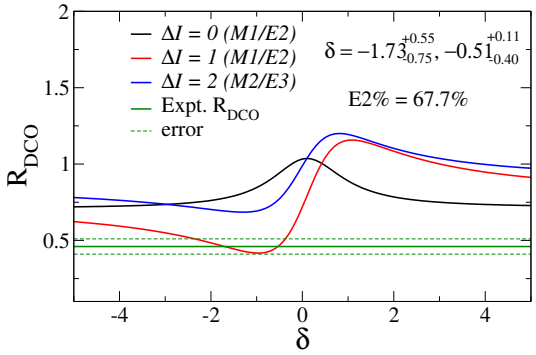

Figure 5.10 The variation of R_{DCO} with the mixing ratio (δ) of different multipoles (L) for 815.4-keV transition.

The 1020.1-keV (Fig. 5.3) transition was observed to decay to the 3694.5-keV level and this transition is identified as a stretched $E2$ transition. The level at energy 3694.5

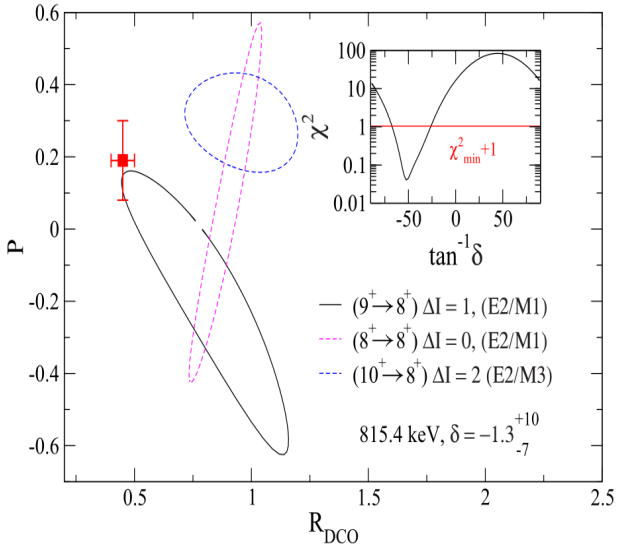

Figure 5.11 The variation of linear polarization (P) as a function of R_{DCO} at different values of mixing ratio (δ) for 815.4-keV transition. The inset shows the χ^2 vs $\tan^{-1}\delta$ plot giving the mixing ratio δ = -1.3$^{+10}_{-7}$.

keV was also found to be connected with band b6 through two $M1$ γ-transitions of energy 394.4- and 655.1- keV (Fig. 5.9). The 850.3 keV γ-transition was observed to decay to 1391.4-keV level in the previous work. We have placed this transition at level energy 3300.1 keV, because this transition is observed in the 655.3-keV gated spectrum. The 812.3-, and 764.6-keV (Fig. 5.12) transitions at level energies 3262.0 and 3214.5 keV, respectively, were observed to decay to the 2450.0 keV-level of band b7. The 812.3 and 764.4 keV transitions are assigned as quadrupole nature based on DCO measurements. The transitions 1368.8 (Fig. 5.3) and 544.0 keV are observed to decay to the 3084.5- and 3909.5-keV level of band b7. The 1368.8 keV γ-transition is assigned as $E2$ multipolarity.

The band b8 is extended by the placement of 949.9-keV stretched $E2$ γ-transition at the level 3507.7 keV. The earlier observed band b8 was found to decay to the ground state through $\Delta I = 0, 2$ transitions [170]. We have observed two new γ-transitions 579.7- (Fig. 5.13) and 862.5- keV decaying from band b8 to band b6 (even member of the gamma band). This band arises from the contribution by coupling of 2qp ($\pi[g_{7/2}]^2 + \pi[g_{7/2}d_{5/2}]$)

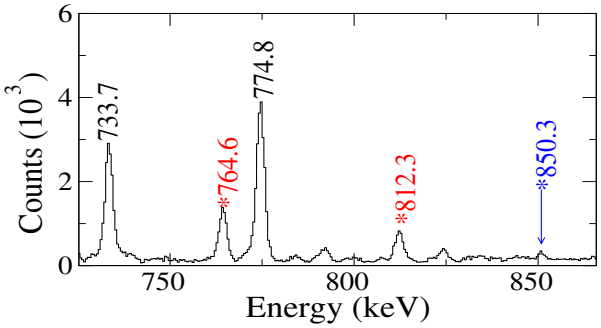

Figure 5.12 Prompt γ-γ coincidence spectra with gate on 655.3 keV transition. The transition labeled in blue color was observed to decay at a level energy of 1391.4 keV. In the present work, this transition is observed to decay to the level of 2450.0 keV.

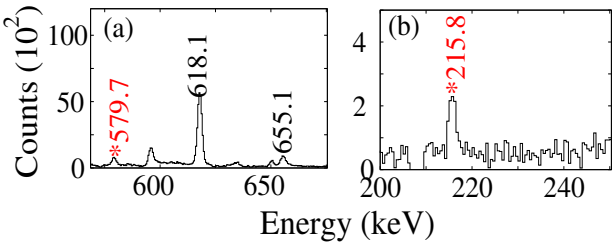

Figure 5.13 Prompt γ-γ coincidence spectra obtained from the gate on 635.5-(a) and 901.2-keV (b) transitions.

with quadrupole phonon [155]. Such bands have been observed in all even Te isotopes with A $\approx$ 112-130 [155].

Two new feeding transitions with energies 215.8-, and 645.3-keV (Fig. 5.13, 5.14) have been observed between band b8 and b9. The 1034.7 keV transition (decay from band b9 to b1), which was previously reported as magnetic type [170], was observed as an electric type. In Fig. 5.15, the R_{DCO} vs. linear polarization plot has been plotted for 1034.7-kev transition, the value of δ obtained from the R_{DCO}-polarization method gives δ = -0.10$^{+15}_{-20}$. We have also observed a 471.2-keV γ-transition (Fig. 5.16), that connects the (9^-) level to the 7^- state of the band b9. A very weak transition of 802-keV has been observed to decay to the 5^+ level of band b7 (odd member of gamma band) from the 7^- level of band b9.

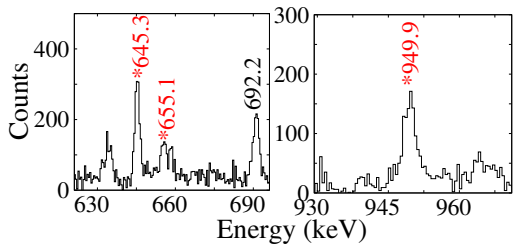

Figure 5.14 Prompt γ-γ coincidence spectra obtained from the gate on 1123.1-keV transitions.

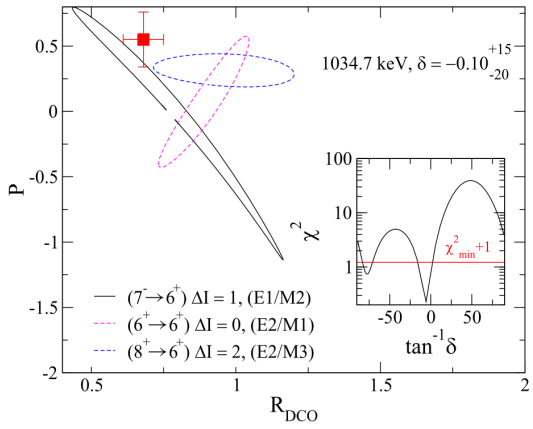

Figure 5.15 The variation of linear polarization (P) as a function of R_{DCO} at different values of mixing ratio(δ) for 1034.7-keV transition.

5.4 Discussions

A. Octupole correlation

The band b2 is based on two quasi-neutron $\nu h_{11/2}d_{5/2}$ configurations. Both orbitals differ in orbital angular momentum as well as total angular momentum by $3\hbar$, resulting in reflection-asymmetric structure. Several electric dipole transitions are observed between band b2 to b1 and between band b4 to b2. There are two criteria for determining the octupole deformation, both of which measure the extent of interleaving between the positive- and negative-parity states [173]. The first criterion measures the ratio of the

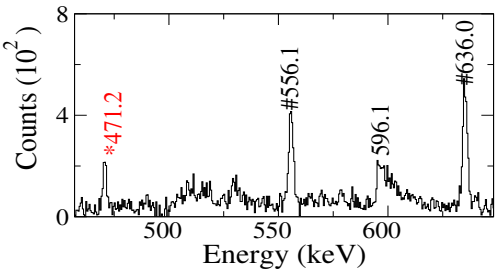

Figure 5.16 Prompt γ-γ coincidence spectra obtained from the gate on 1034.7-keV transition. The 636.0 keV transition could not be placed because of unsatisfactory coincidence. The placement of 556.1- and 636-keV gamma transitions represented by # symbol could not be resolved in the present work.

rotational frequency of positive and negative parity bands, which is defined as [174, 175]:

$$\frac{\omega^-(I)}{\omega^+(I)} = 2\frac{E(I+1)^- - E(I-1)^-}{E(I+2)^+ - E(I-2)^+}\,(I_{even}) \tag{5.6}$$

$$\frac{\omega^-(I)}{\omega^+(I)} = 0.5\frac{E(I+2)^- - E(I-2)^-}{E(I+1)^+ - E(I-1)^+}\,(I_{odd}) \tag{5.7}$$

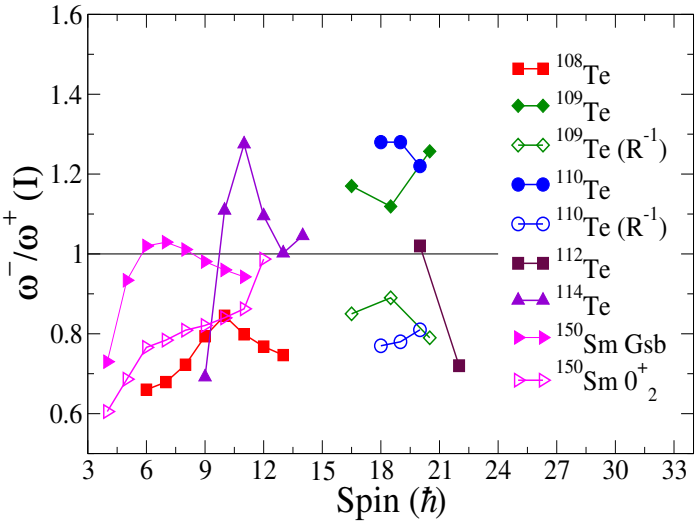

Figure 5.17 The rotational frequency ratio between the negative and positive parity bands as a function of spin for nuclei in different mass regions.

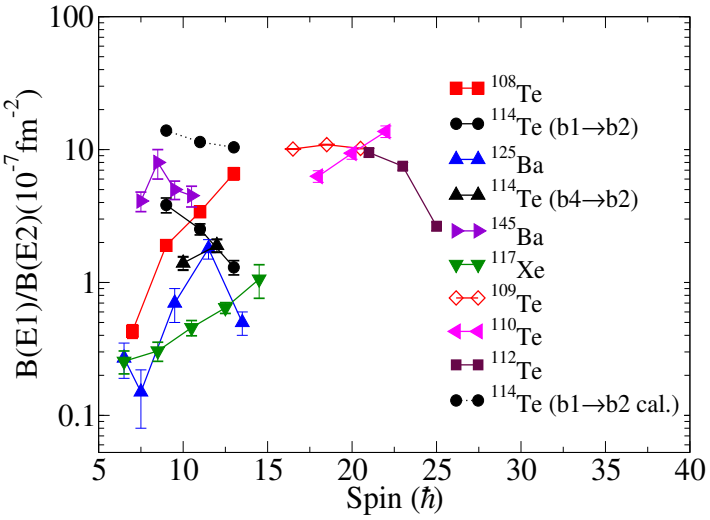

Figure 5.18 Experimental B($E1$)/B($E2$) ratios with respect to spin have been plotted for different nuclei.

The value of this ratio is equal to 1 for a perfect reflection-asymmetric nucleus. This ratio is compared with other light mass tellurium isotopes (see Fig. 5.17). It is observed that the ω^-/ω^+ ratio for the yrast band (b1) coupled with octupole band b2 lies between 0.69 and 1.27. The results for ^{109}Te and ^{110}Te show a stark contrast. In these two nuclei, positive-parity states gradually decrease and merge with negative-parity states. When the inverse ratio R^{-1} is plotted for the states in ^{109}Te and ^{110}Te, the result looks similar to those for R in ^{108,112}Te. Another parameter to describe the octupole deformation is the energy difference between the positive and negative parity bands, which is defined as follows [176]:

$$\Delta E(I) = E_-(I) - \frac{E_+(I+1) + E_+(I-1)}{2} \tag{5.8}$$

In the limit of stable octupole deformation, the value $\Delta E(I)$ is close to zero. The most important experimental signature of octupole correlation is the observation of enhanced $E1$ transition. We have measured the B($E1$)/B($E2$) ratio of four new γ transitions and one old transition interconnected between band b2 to b1 and band b4 to b2. The observed value of

B($E1$)/B($E2$) lies between ^{108}Te [165] and ^{145}Ba [177] (see Table 5.3 and Fig. 5.18). To explore the octupole correlations in ^{114}Te, the potential energy surface in the (β_{20}, β_{30}) plane is calculated by the covariant density functional theory (CDFT) in 3D lattice space [178–181] and shown in Fig. 5.19. The relativistic point-coupling density functional PC-PK1 [182] is used, and the pairing correlations are taken into account with the BCS method. The neutron pairing strength -480 MeV·fm^3 is determined by reproducing the empirical pairing gap of ^{114}Te, and the proton pairing strength -480 MeV·fm^3 is also adopted. For the 3D lattice space, the mesh sizes and the grid numbers along the x, y, and z axes are chosen as 1 fm and 26, respectively. The size of the space adopted here is sufficient to obtain converged solutions. In Fig. 5.19, the potential energy surface exhibits a minimum at (β_{20}, β_{30}) = (0.189,0), and it is rather soft in the octupole direction. The energy rise is about 0.2 MeV with a change in octupole deformation of 0.05. Hence, the enhanced $E1$ transitions between positive and negative parity bands of ^{114}Te can be expected due to octupole soft nature. According to the relativistic Hartree-Bogoliubov model-based quadrupole- octupole collective Hamiltonian (QOCH-RHB)calculations, the value of the B($E1$)/B($E2$) ratios are calculated for the bands b1 and b2 and shown in Fig. 5.18. The calculated values are higher than the experimental value.

Table 5.3 Measured B($E1$)/B($E2$) ratios and deduced electric dipole moment in ^{114}Te.

$E\gamma$ (keV)	$I_i \rightarrow I_f$	B($E1$)/B($E2$)[a] ($10^{-7} fm^{-2}$)	|D$_0$| (efm)
425.3	$9^- \rightarrow 8^+$	3.83 (49)	0.081 (7)
384.2	$11^- \rightarrow 10^+$	2.52 (30)	0.066 (6)
516.5	$13^- \rightarrow 12^+$	1.30 (16)	0.047 (4)
843.2	$10^+ \rightarrow 9^-$	1.42 (16)	0.049 (4)
765.8	$12^+ \rightarrow 11^-$	1.91 (21)	0.057 (4)

[a]The values are measured by using the following formula:

$$\frac{B(E1)}{B(E2)} = \frac{1}{1.3 \times 10^6} \frac{E_\gamma^5(E2) I_\gamma(E1)}{E_\gamma^3(E1) I_\gamma(E2)} [fm^{-2}]$$

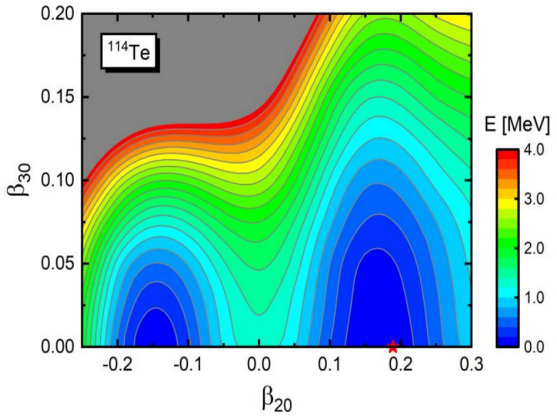

Figure 5.19 The potential energy surface of ^{114}Te calculated using CDFT in 3D lattice space. The energies are normalized to the ground state with (β_{20}, β_{30}) = (0.189,0). The contour interval is 0.2 MeV.

It is also important to estimate the intrinsic dipole moment D_0, which can be calculated by using the following formula [64]:

$$D_0 = Q_0 \left[\frac{5}{16} \frac{B(E1)}{B(E2)} \right]^{1/2} \tag{5.9}$$

Where Q_0 is the intrinsic electric quadrupole moment. We have calculated Q_0 = 236 efm^2 by using B($E2$) value . The observed value of the electric dipole moment in ^{114}Te is comparable to light Te isotopes [165].

B. Shell Model Interpretation

The structure of ^{114}Te is studied in the $50-82$ valance space above the core $^{100}_{50}$Sn using SN100PN effective interaction [115]. This model space consists of five proton and neutron orbitals labeled as $g_{7/2}$, $d_{5/2}$, $h_{11/2}$, $d_{3/2}$, and $s_{1/2}$. The single-particle energies of proton orbitals are 0.8072, 1.5623, 3.6051, 3.3160, and 3.2238 MeV, while those of neutron orbitals are -10.6089, -10.2893, -8.8152, -8.7167, and -8.6944 MeV, respectively. The residual two-body matrix elements of this interaction are obtained through the G-matrix approach derived from charge density (CD)-Bonn nucleon-nucleon potential [183].

The interaction consists of three parts: proton-proton (pp), neutron-neutron (nn), and neutron-proton (np). Coulomb interaction between the protons is also considered. The details regarding the matrix elements can be found in Ref. [115]. To diagonalize the Hamiltonian, we have used the standard shell model code KSHELL [108]. To deal with the computational complexity associated with large dimensions, the present shell model calculations are performed with truncation. We have tried to minimize the truncation, and it is employed only in the case of neutron orbitals, *i.e.*, we put a minimum of 4 particles in the lowest $\nu g_{7/2}$ orbital. The reduced electromagnetic transition strengths are calculated with standard effective charges for proton and neutron as $e_p = 1.5$ and $e_n = 0.5$ while the effective g factors, used for them, are $g_l^p = 1.0, g_s^p = 5.585$ and $g_l^n = 0.0, g_s^n = -3.826$ respectively.

The energy levels of ^{114}Te obtained from the experiment are compared with the corresponding levels calculated from the shell model in Fig. 5.20. In the calculated energy spectra of ^{114}Te, the 2_1^+ state appeared 170 keV below the corresponding experimental level. The measured energy difference between 2_1^+ and 4_1^+ states is 774.8 keV, while the SM evaluated value is 557 keV. The experimental 3_1^+ state is at 1.795 MeV and the calculated one lies very close to it, i.e., at 1.759 MeV energy. This shows that the SM results for low-lying states are in good agreement with the experimental data and observed within a difference of a few hundred keV compared to the measured values. However, the high-spin states are suppressed to lower energies compared to their experimental counterparts. A similar pattern is also observed in the case of negative-parity states as shown in Fig. 5.20. The SM calculations in heavier Te isotopes ($A \geq 124$) with the same interaction have been performed in [184, 185]. The observed low-spin states in $^{128-131}$Te fairly agree with the SM results while the energies of high-spin states still deviate from the experimental data. These isotopes are close to the $N = 82$ shell closure, are well described by the SM calculation. As we go below $N = 82$ magic number, for $^{124-127}$Te [185], more differences

between experimental and calculated energies of both the positive and negative-parity states are observed. It is found that the rms deviation from the experimental data increases as one moves from ^{127}Te to ^{124}Te. As expected, similar discrepancies are seen in the SM results of ^{114}Te.

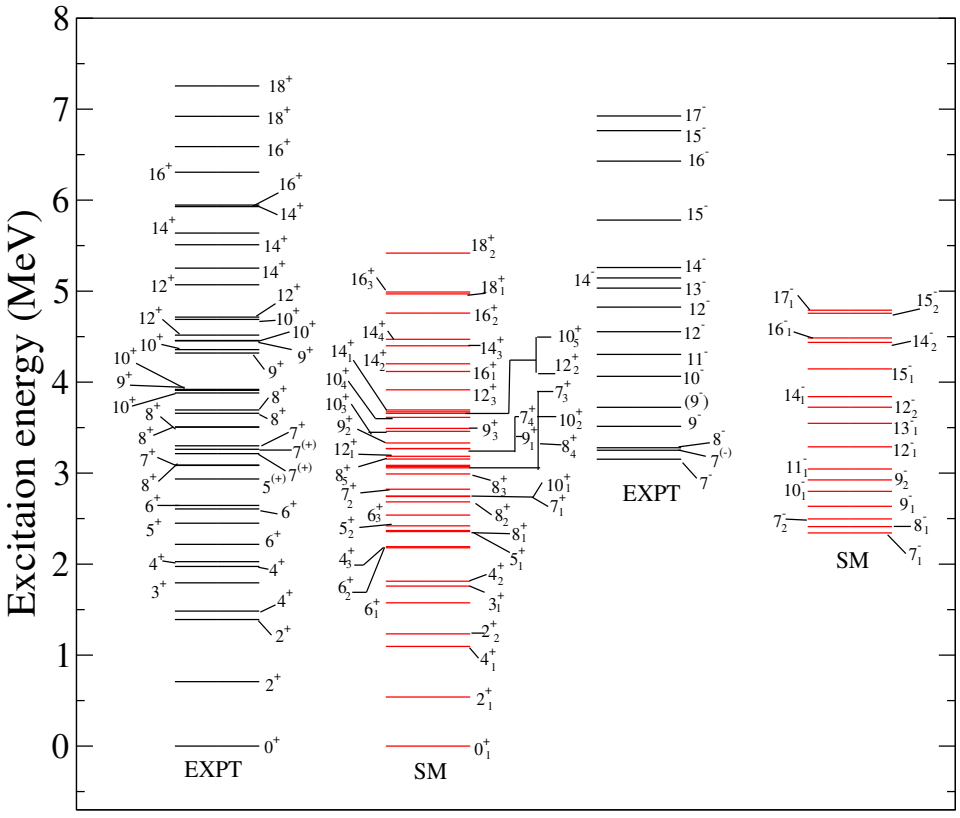

Figure 5.20 Comparison between experimental and calculated energy levels for ^{114}Te.

The wave functions of various states of ^{114}Te arise from a large mixing of different configurations and show collective behavior. The major components to the wave function configurations of the first positive-parity even-spin states (band b1) come from $[\pi(g^2_{7/2})/\pi(g^1_{7/2},d^1_{5/2})\otimes\nu(g^6_{7/2}d^4_{5/2}h^2_{11/2})]$. In the calculation, the 10^+_1 state is associated with the ground state band because it shows a similar neutron configuration like other members of the band b1. The calculated values of B($E2$) agree very well with the experi-

mental value (see Table 5.4). It is observed that the value of B($E2$) for 10_1^+ to 8_1^+ decreases significantly compared to the low-spin counterparts. The same is well reproduced in the calculation. The small B($E2$) value at spin 10_1^+ indicates a possible transition from collective to non-collective behavior. On the other hand, the values of B($E2$) increase thereafter and attain values similar to those of the low-spin part and almost remain constant. A non-collective oblate state was predicted by Paul *et al.* [152] at spin $16\hbar$ for all lighter Te isotopes with $A \leq 122$ based on $[\pi(g_{7/2}^2)_{6^+} \otimes \nu(h_{11/2}^2)_{10^+}]$ configuration. In Fig. 2(a) of ref. [152] the rigid rotor plots have been plotted for ^{114}Te, which shows a change in alignment at states 16_1^+. Since, the shell model calculation is not in good agreement with experimental values at higher spin, so we have performed potential energy surface (PES) calculations with the Ultimate Cranker code (UC) [127, 128, 186, 187]. The potential energy surface plot for 16_1^+ state has been shown in Fig. 5.21 with parity and signature (π, α) = (+,0). The minimum was found at $\varepsilon_2 = 0.15, \gamma = 61.9^\circ$, which shows the non-collective oblate.

Table 5.4 Comparision of B($E2$) values for the band b1 obtained from the experiment and shell model calculations.

$E\gamma$ (keV)	$I_i \rightarrow I_f$	Expt. B($E2$)[a] (W.u.)	calculated B($E2$) (W.u.)
708.7	$2_1^+ \rightarrow 0_1^+$	34.0 (30)	18.3
774.8	$4_1^+ \rightarrow 2_1^+$	28.7 (30)	26.7
733.7	$6_1^+ \rightarrow 4_1^+$	42.7 (80)	24.6
871.2	$8_1^+ \rightarrow 6_1^+$	25.1 (90)	22.1
831.3	$10_1^+ \rightarrow 8_1^+$	0.93 (11)	0.8
596.1	$12_1^+ \rightarrow 10_1^+$	54.2 (128)	28.5
736.9	$14_1^+ \rightarrow 12_1^+$	-	28.4
692.2	$16_1^+ \rightarrow 14_1^+$	-	21.5
975.6	$18_1^+ \rightarrow 16_1^+$	-	16.0

[a]Experimental values are taken from the Ref. [156]

For the band b5 major contribution comes from $[\pi(g_{7/2}^2) \otimes \nu(g_{7/2}^4 d_{5/2}^4 h_{11/2}^4)]$ configuration. Here, the calculated 10_2^+ is considered as the band-head of band b5. The calculated

B($E2$) values are almost constant $\sim$ 26 W.u. across the band, which confirms the rotational behavior as reported in [170].

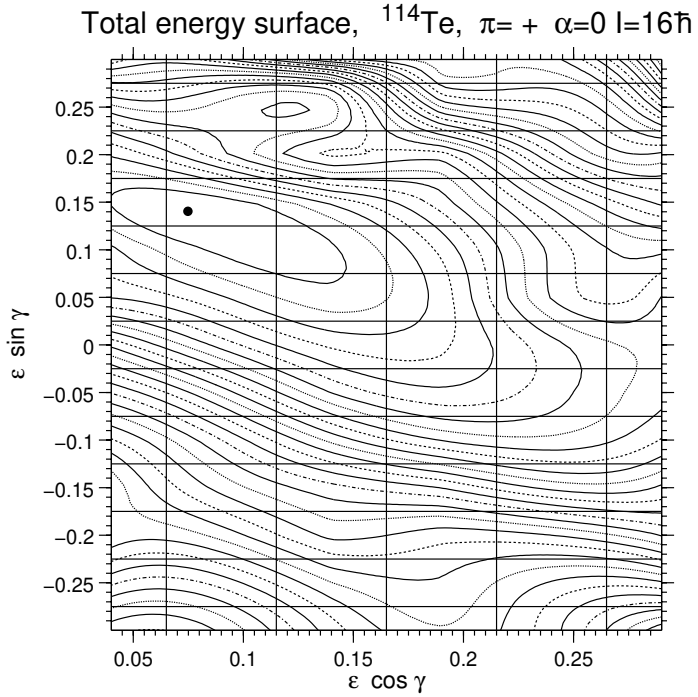

Figure 5.21 Potential energy surface plot from the ULTIMATE CRANKER for ^{114}Te at $I = 16^{+}_{1}\hbar$.

The dominant wave function configuration for the band b2 and b3 is $[\pi(g^2_{7/2})/\pi(g^1_{7/2}d^1_{5/2})\otimes \nu(g^5_{7/2}d^4_{5/2}h^3_{11/2})]$. As shown in Fig. 2(a) of ref. [152], a change in alignment was also observed at spin 14^{-}_{2} based on $[\pi(g^2_{7/2})_{6^+}\otimes\nu[(d_{5/2})(h_{11/2})]_{8^-}]$. The state was probed through PES calculation using the UC menu, which indicates a potential minimum at $\varepsilon_2 = 0.16, \gamma = 62.2^{\circ}$ (see Fig. 5.22). This indicates a terminating state with non-collective oblate. A small sequence consisting of 491.1- and 591.0-keV γ transitions feed at spin 10^{-} of band b3 are supposed to evolve from the same configuration. Here we have considered 12^{-}_{1} and 14^{-}_{1} states to be associated with this cascade. The small sequence of γ-transitions which feeds at 13^{-} spin of band b2 are supposed to evolve from the $[\pi(g^2_{7/2})\otimes\nu(g^5_{7/2}d^3_{5/2}h^4_{11/2})]$ configuration except 18^{+} state, which evolves from the $[\pi(g^2_{7/2})\otimes\nu(g^4_{7/2}d^4_{5/2}h^4_{11/2})]$.

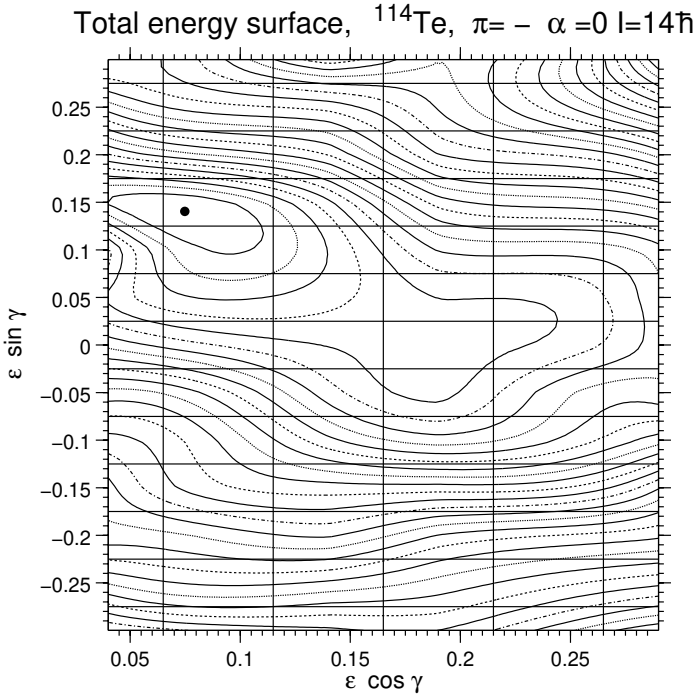

Figure 5.22 Potential energy surface plot for ^{114}Te at $I = 14^{-}_{2}\hbar$.

The calculated 8^{+}_{3}, 10^{+}_{3}, 12^{+}_{3} and 14^{+}_{3} states with $[\pi(g^{2}_{7/2}) \otimes \nu(g^{5}_{7/2}d^{3}_{5/2}h^{4}_{11/2})]$ configuration are proposed to be associated with band b4. The corresponding calculated B($E2$) values are shown in the Table 5.5. The B($E2$) values are very high, which confirms the collective behavior of band b4.

The dominant wave function for band b8 is $[\pi(g^{2}_{7/2}) \otimes \nu(g^{5}_{7/2}d^{3}_{5/2}h^{4}_{11/2})]$. Band b8 feeds on both the collective quadrupole band b1 and the γ band b6. Here, the calculated 6^{+}_{3}, 8^{+}_{4}, and 10^{+}_{4} states are assumed to be associated with the band b8. The calculated B($E2$) values for the $8^{+}_{4} \rightarrow 6^{+}_{3}$ and $10^{+}_{4} \rightarrow 8^{+}_{4}$ transitions are 6 and 0.15 W.u., respectively. This shows that the 8^{+}_{4} state has a collective neutron structure whereas the 10^{+}_{4} state has a non-collective character, which is in accordance with the proposed B($E2$) values by Grinberg *et al.* [155]. The calculated B($E2$) value for the $10^{+}_{1} \rightarrow 8^{+}_{4}$ state (corresponding to 412.4-keV γ-transition interconnecting the bands b1 and b8) has been registered to be remarkably small (0.01 $e^{2}fm^{-4}$), in contrast to the observed B($E2$) value of 20 W.u.

The band b9 are supposed to be evolved from the $[\pi(g^2_{7/2}) \otimes \nu(g^5_{7/2}d^4_{5/2}h^3_{11/2})]$ configuration with large value of B($E2$) (20.7 W.u.).

Table 5.5 B($E2$) transition strength for the observed transition in ^{114}Te .

$E\gamma$ (keV)	$I_i \rightarrow I_f$	calculated B($E2$) (W.u.)
Band b4		
698.9	$10^+_3 \rightarrow 8^+_3$	14.6
713.4	$12^+_3 \rightarrow 14^+_3$	25.3
568.3	$14^+_3 \rightarrow 12^+_3$	26
Band b5		
807.9	$12^+_2 \rightarrow 10^+_2$	28.7
820.7	$14^+_2 \rightarrow 12^+_2$	26.8
797.3	$16^+_2 \rightarrow 14^+_2$	24.1
Band b7		
655.3	$5^+_1 \rightarrow 3^+_1$	12.3
634.6	$7^+_2 \rightarrow 5^+_1$	6.8
825.0	$9^+_1 \rightarrow 7^+_2$	20.5
Band b8		
901.2	$8^+_4 \rightarrow 6^+_3$	6.0
949.9	$10^+_4 \rightarrow 8^+_4$	0.15
Band b9		
471.2	$9^-_2 \rightarrow 7^-_2$	20.7
for other levels		
666.5	$18^+_2 \rightarrow 16^+_3$	0.84
658.9	$16^+_3 \rightarrow 14^+_4$	0.71
1265.7	$4^+_3 \rightarrow 2^+_1$	-
812.3	$7^+_3 \rightarrow 5^+_1$	0.2
850.3	$7^+_4 \rightarrow 5^+_1$	-
1368.8	$9^+_3 \rightarrow 7^+_2$	-
1020.1	$10^+_5 \rightarrow 8^+_5$	2.5
1049.4	$8^+_5 \rightarrow 6^+_2$	-

The major contribution for band b6 comes from the $[\pi(g^2_{7/2}) \otimes \nu(g^6_{7/2}d^4_{5/2}h^2_{11/2})]$ configuration. Here, the 4^+_2 state is considered to be associated with the band b6 because of similar neutron and proton configurations. The dominant wave function configuration of 3^+_1 state of band b7 is $[\pi(g^2_{7/2}) \otimes \nu(g^6_{7/2}d^4_{5/2}h^2_{11/2})]$. Both 5^+_1 and 9^+_1 states appear from a wave function configuration of $[\pi(g^2_{7/2}) \otimes \nu(g^5_{7/2}d^3_{5/2}h^4_{11/2})]$. Here, the 7^+_2 state is assumed

to be associated with the band b7 because it has the same configuration as 5_1^+ and 9_1^+ states, and also the B($E2$) transition strengths between these states are high, which shows collective behavior (see table 5.5).

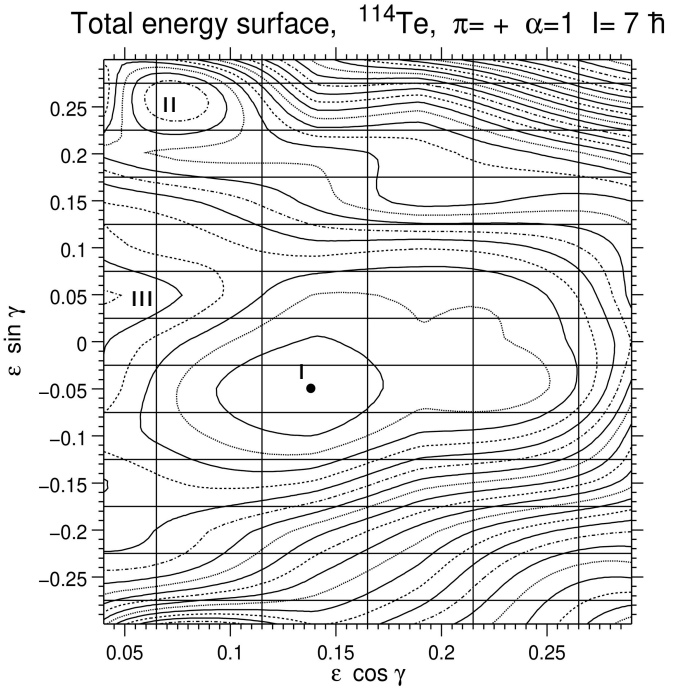

Figure 5.23 Potential energy surface plot from the ULTIMATE CRANKER for ^{114}Te at $I = 7\hbar$. The calculation predicts three minimum which are indicated by I, II, and III.

The calculated states at 7_1^+, 7_3^+ and 7_4^+ evolve from the $[\pi(g_{7/2}^2) \otimes \nu(g_{7/2}^6 d_{5/2}^4 h_{11/2}^2)]$, $[\pi(g_{7/2}^2) \otimes \nu(g_{7/2}^4 d_{5/2}^4 h_{11/2}^4)]$ and $[\pi(g_{7/2}^2) \otimes \nu(g_{7/2}^5 d_{5/2}^5 h_{11/2}^2)]$ configuration respectively and can be associated with the experimentally observed 7^+ states at energies 3214.5-, 3262.0-, and 3300.1-keV, which are nearly degenerate. However, degeneracy in excitation energy of the calculated states at 7_1^+, 7_3^+, and 7_4^+ are not reproduced. Similar degenerate states at the same spin were also observed in ^{126}Te [188] with level energies 2901.4-, 2968.2-, and 3064.6-keV, respectively. Fig. 5.23 shows the PES plot at $I = 7\hbar$ with parity and signature(π, α) = (+,1) built with $[\pi(+,1), \nu(+,0)]$. The most favored minimum

occurs at $\varepsilon_2 = 0.14, \gamma = -19^\circ$ along with two other minima at $\varepsilon_2 = 0.26, \gamma = 74^\circ$ and $\varepsilon_2 = 0.06, \gamma = 49.2^\circ$ respectively.

The 4^+ and 5^+ states which are fed to the ground state band at level 708.7- and 1483.5-keV respectively are supposed to be generated from the $[\pi(g^2_{7/2}) \otimes \nu(g^5_{7/2}d^3_{5/2}h^4_{11/2})]$. A couple of 9^+ states at level energies 4320.0- and 4453.4-keV respectively decay at level energies 3504.6- and 3909.5-keV of band b6 and b7 are associated with $[\pi(g^2_{7/2}) \otimes \nu(g^4_{7/2}d^4_{5/2}h^4_{11/2})]$ and $[\pi(g^1_{7/2}d^1_{5/2}) \otimes \nu(g^5_{7/2}d^4_{5/2}d^1_{3/2}h^2_{11/2})]$ respectively.

The calculated 8^+_5 and 10^+_5 states from the $[\pi(g^2_{7/2} \otimes \nu(g^4_{7/2}d^4_{5/2}h^4_{11/2})]$ and $[\pi(g^2_{7/2} \otimes \nu(g^5_{7/2}d^3_{5/2}h^4_{11/2})]$ configuration respectively are proposed to be associated with the experimentally observed 8^+ and 10^+ states at level energies 3694.5- and 4714.6-keV. The calculated B($E2$) value for this transition is 2.5 W.u., which shows the non-collective nature of the 10^+_5 state.

5.5 Summary

The level scheme of ^{114}Te has been reviewed and extended by the addition of thirty-five new transitions. The spin-parity of different states has been established on the basis of directional correlation ratio and polarization measurements. The observation of enhanced $E1$ transitions between bands b2 and b1, b4 and b2 indicates the presence of octupole correlation in this nucleus, which is further supported by the results of CDFT calculation where ^{114}Te is shown to be soft along octupole direction. In addition, all the observed bands were probed within the framework of shell model calculation. Theoretical results were mostly found to be in agreement with the observed results in the low-spin regime of the level scheme. However, with the increase in spin, the calculated outcomes from the shell model calculation are found to deviate from the observed results. Hence, at some higher spin states, where the non-collectivity was predicted by Paul *et al.* were discussed with the help of the Ultimate Cranker model. The calculated results from UC

menu were also able to describe the existence of degenerate states for the 7^+ state. Thus, ^{114}Te presents a rich laboratory to study collective and non-collective excitation along with the prevalence of octupole softness.

*****The authors thank the Cyclotron operations staff and VECC INGA members for their support. The authors would like to thank Z.P.Li. and Ruonon Mao for the fruitful discussion on octupole correlation. INGA is partially funded by the Department of Science and Technology, Government of India (No. IR/S2/PF-03/2003-II). M.P. would also like to thank Nidhi Goel, Aalakh Kumar and Atreyee Dey for their valuable advice and support. This work was carried out under the contract PN 23.21.01.06 sponsored by the Romanian Ministry of Research, Innovation and Digitization. S.R. is grateful to the SERB-DST for the financial support under the core research grants (File Number: CRG/2020/003370).